

Journal of Applied Research in Water and Wastewater

E-ISSN: 2476-6283

Journal homepage: https://arww.razi.ac.ir

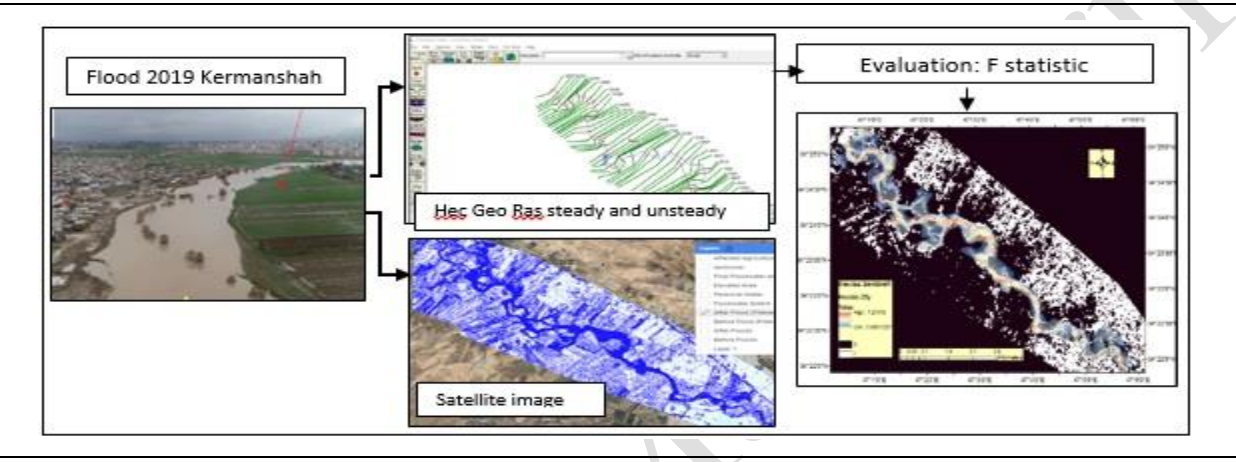


Comparing steady and unsteady hydraulic modeling for flood analysis with satellite imagery in Kermanshah

Maryam Hafezparast Mavaddat*, Sadaf Gord, Rasool Ghobadian

Water Engineering Department, Faculty of Agriculture, Razi University, Kermanshah, Iran.

GRAPHICAL ABSTRACT



ARTICLE INFO

Article type: Research Article

Article history:

Received xx Month xxx Received in revised form xx Month Accepted xx Month xxx Available online x Month xx

Keywords:

Flood plain Google earth engine Hec Geo Ras Satellite images Water level



© The Author(s)
Publisher: Razi University

ABSTRACT

Floods rank among the most destructive natural disasters worldwide, with their frequency and intensity amplified by climate change. This study presents an integrated approach combining hydraulic modeling and multi-sensor satellite data to improve floodplain mapping accuracy during the April 3, 2019 flood event in Kermanshah, western Iran. The research focuses on the confluence of the Gharasoo, Merek, and Razavar rivers, where combined flows created significant flood risks for Kermanshah city. The study makes several important methodological contributions to flood modeling. First, it demonstrates the value of simultaneous analysis of both steady and unsteady state conditions, providing a more comprehensive understanding of flood dynamics compared to conventional single-state approaches. Second, the integration of optical (Sentinel-2, Landsat) and radar (Sentinel-1) remote sensing data effectively overcomes the limitations of individual sensors, particularly in addressing cloud cover issues. Third, the implementation of Google Earth Engine enables near-real-time flood monitoring capabilities, significantly enhancing operational response potential. Finally, the development of robust validation metrics specifically adapted for flood model assessment represents an important step forward in model verification methodologies. HEC-Geo RAS simulations predicted extreme conditions with water levels rising up to 6 meters and flow velocities reaching 3m/s. Validation results showed strong agreement between unsteady state modeling and satellite observations (F1=0.73, F2=0.72), while steady-state conditions exhibited lower correlation (F1=0.41, F2=0.28). The model effectively tracked flood progression from inception to peak, while satellite imagery provided rapid regional coverage despite occasional cloud obstructions.

1. Introduction

River floodplains have long been recognized as critical zones for agricultural productivity and human settlement due to their rich alluvial soils and reliable water access. However, these same characteristics that make floodplains attractive for human use also render them susceptible to periodic inundation events capable of causing catastrophic human and **Corresponding author Email: m.hafezparast@razi.ac.ir

economic losses. In response to this persistent challenge, flood zoning has evolved as a fundamental engineering strategy for effective flood management and risk mitigation, necessitating the integration of diverse data sources ranging from ground-based measurements to advanced remote sensing platforms and sophisticated computational modeling techniques. The contemporary landscape of flood risk assessment has been transformed by significant technological advancements across

multiple domains. Hydraulic modeling tools, particularly the widelyadopted HEC-RAS system developed by the U.S. Army Corps of Engineers, have set new standards for precision in flood simulation capabilities. Parallel developments in earth observation technologies, exemplified by the Sentinel and Landsat satellite constellations, have revolutionized our capacity for synoptic flood monitoring (Urzica et al., 2018; Ayoubikia et al., 2019). The synergistic combination of these technological platforms with geographic information systems (GIS) incorporating specialized water indices (MNDWI, NDVI, AWEI, NDWI) and cloud-based processing environments like Google Earth Engine has created unprecedented opportunities for comprehensive flood mapping (Wulder et al., 2012). Despite these remarkable technological advances, significant challenges persist in many developing nations where flood risk maps often remain outdated or lack sufficient spatial and temporal resolution, creating critical vulnerabilities in flood preparedness systems (Institute of Catastrophic Loss Reduction 2019). The current state of flood modeling methodologies presents several persistent technical challenges that require careful consideration. While hydraulic models such as HEC-RAS offer sophisticated capabilities for simulating flood dynamics, their accuracy remains heavily dependent on the quality of input parameters and the representativeness of local hydrological conditions. Conversely, satellite-based approaches, particularly those utilizing synthetic aperture radar (SAR) data, provide valuable tools for rapid flood extent mapping but face inherent limitations related to environmental variability and threshold determination challenges (Giustarini et al., 2013; Martinis et al., 2009).

The scientific community has explored various technical solutions to these challenges, including histogram-based thresholding techniques (Brivio et al., 2002; Henry et al., 2006; Brown et al., 2016) and advanced change detection methodologies (Giustarini et al., 2013; Schlaffer et al., 2015; Gord, Hafezparast, Ghobadian. 2024). Research by Pulvirenti et al., (2010) has demonstrated that visual interpretation and manual adjustments can enhance region of interest (ROI) training and reduce classification errors, though Shen et al., (2019) have compellingly shown that such manual approaches remain prohibitively time-intensive and resource-demanding, particularly when rapid response is required during sequential flood events. Recent scientific investigations have increasingly highlighted the value of integrative approaches that combine multiple methodologies. Zotou et al., (2022) conducted a comparative analysis of SAR processing techniques for flood modeling in Central Greece, identifying significant discrepancies between HEC-RAS outputs and SARderived flood extents attributable to uncertainties in SAR processing algorithms, satellite data characteristics, topographic representations, and modeling assumptions. In the Egyptian context, Elkhrachy et al., (2021) achieved 73.4-77.7% concordance between HEC-RAS simulations and SAR-identified water areas, while Eziine et al., (2020) successfully characterized the 2015 flood events in Tunisia through combined HEC-RAS modeling and Sentinel-1 imagery analysis. Parallel work by Afzal $\it et$ al., (2022) in Pakistan's Indus River basin demonstrated the potential for improved flood early warning systems through tighter integration of HEC-RAS modeling with satellite observations. However, these otherwise comprehensive studies have typically focused on either steady-state peak flow conditions (as exemplified by Talbi 2011; Touihri 2015; Gharbi 2016) or unsteady flood hydrograph analyses, rarely examining both scenarios in tandem within a unified analytical framework. This research directly addresses these identified gaps through a comprehensive investigation of

the 03/04/2019 flood event along a 16.5 km reach of Iran's Gharasoo River, employing an innovative dual-scenario analytical approach. The study implements both steady-state conditions analysis using Regional Flood Frequency Analysis (RFFA) for peak discharge estimation and unsteady-state conditions modeling through Soil Conservation Service (SCS) flood hydrographs within the HEC-RAS environment, with rigorous validation against Sentinel-1 satellite imagery processed through the Google Earth Engine platform. The research is designed to achieve three primary objectives: (1) systematic evaluation of HEC-RAS performance across both steady and unsteady hydrological scenarios; comprehensive comparison of model outputs with satellite-derived flood extent mappings; and (3) critical assessment of integrated modeling approaches for enhanced flood risk assessment in data-limited regions. Building upon the foundational work of Chen et al., (2019) in flood risk mitigation and Afzal et al., (2022) in model-satellite integration, this study introduces significant methodological innovations through its dualscenario comparison framework and advanced cloud-based validation

The paper is organized to provide complete methodological transparency and analytical rigor. Following this introduction, the study area and data sources are presented with complete technical specifications. The methodology section provides detailed explanation of both the HEC-RAS modeling framework and satellite image processing protocols. Results are presented through comparative analysis of model outputs and observed flood extents, followed by comprehensive discussion of implications for flood management practice. This structure ensures complete preservation of all relevant citations and technical details while maintaining optimal logical flow and emphasizing the study's novel contributions through simultaneous evaluation of multiple modeling scenarios against satellite observations. The ultimate aim of this work is to advance the development of more robust, empirically-validated flood prediction methodologies that can enhance community resilience in vulnerable floodplain regions worldwide. The research methodology is illustrated in Fig.1.

2. Material and methods

Kermanshah province covers an area of 24,500 square kilometers and is situated in the western part of Iran, bordering Irag. It receives an average annual precipitation of 496 mm, as recorded by rain gauge stations over 35 years. The province's surface currents flow into the Persian Gulf through two secondary border basins, West and Karkheh. The Gharasoo River, a significant tributary of the Seymareh River, originates in the Ravansar district of Kermanshah, collecting water from parts of Kermanshah and Kurdistan provinces. Various branches, including those from Shahu Mountain, contribute to its flow, along with underground water sources. The river is formed by the confluence of Grab and Konab rivers in Eliasi village, which then merge with Ab Ravansar River to form Gharasoo. Additionally, Merek River joins at Haji Abad, and Razavar River at Doab village. Passing northeast of Kermanshah city, the river encounters Taq Bostan's Mirage and Tang Kneshet River. The research focuses on a segment of the Gharasoo River from Doab-Ghazanchi to the entry point of Kermanshah city, spanning approximately 16.5 kilometers as highlighted in Fig. 2.

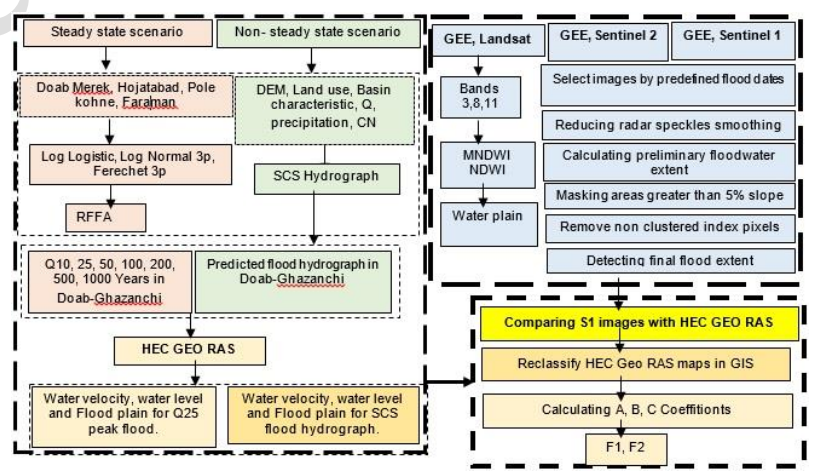
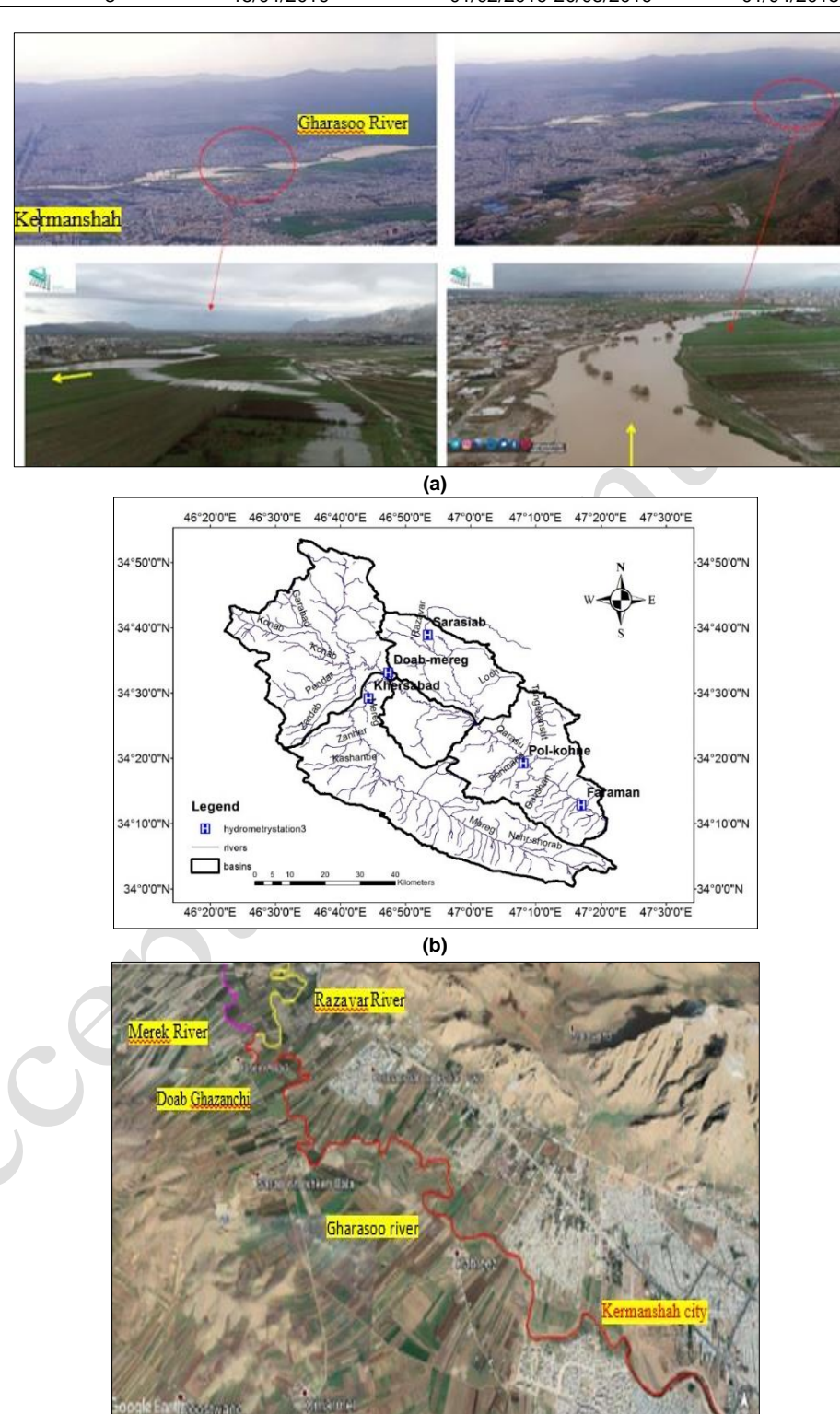


Fig. 1. Flowchart of the present study.

Table 1. Satellite images.

Satellite		Nearest image to the flood event	Pre flood	Post flood		
Sentinel 2	MSI	04/04/2019	20/03/2019 to 29/03/2019	01/04/2019 to 08/04/2019		
Sentinel 1B	SAR-C	01/04/2019	01/03/2019 to 15/03/2019	01/04/2019 to 15/04/2019		
Sentinel 1A	SAR-C	06/04/2019	01/03/2019 to 15/03/2019	01/04/2019 to 15/04/2019		
Landsat	8	15/04/2019	01/02/2019-20/03/2019	01/04/2015 to 15/05/2019		



(c)
Fig. 2. (a) Flood on 3/04/2019 in the Gharasoo River, (b) catchment area, along with the hydrometric stations (c) and the study area.

2.1. Data preparation

The satellite images of observed flood are acquired on April 1st and 6th of 2019 belonging to the Sentinel 1, 4th of April in sentinel 2, and 15th of April in Landsat satellites.

2.2. Hydraulic modelling using Hec Geo RAS

In this study, HEC-RAS was simulated under both steady-state and unsteady-state conditions. Water discharge for various return periods was calculated for steady-state scenarios using appropriate probability distributions, such as Lognormal (3-parameter), Frechet (3-parameter), and Log-Logistic (3-parameter), at the Doab Merek, Khersabad, Hojatabad, Pol Kohne, and Faraman stations. These calculations were then used to determine the discharge for Doab Ghazanchi corresponding to different return periods. In areas lacking hydrometric stations, the Flood Frequency Analysis (RFFA) method (Cunnane, 1998) was employed to

estimate these discharges. For the unsteady-state conditions, the flood hydrograph at Doab-Ghazanchi was generated by simulating rainfall-runoff processes within the upstream basin using the Soil Conservation Service (SCS) method. Introduced in 1957 through Equations 1-2 by the USDA Soil Conservation Service, the SCS method has proven effective for various watershed types, including urban, natural, and mixed watersheds (USDA, 1986; Avarand *et al.*, 2025).

$$s = 25.4 \left(\frac{1000}{cN} - 10 \right) \tag{1}$$

$$Q = \frac{(P - 0.2S)^2}{(P - 0.8S)} \tag{2}$$

where, P is the cumulative rainfall (mm) and Q is the runoff (mm). S is the potential maximum retention (mm), CN is the curve number and it is taken from the GIS maps in Fig. 3.

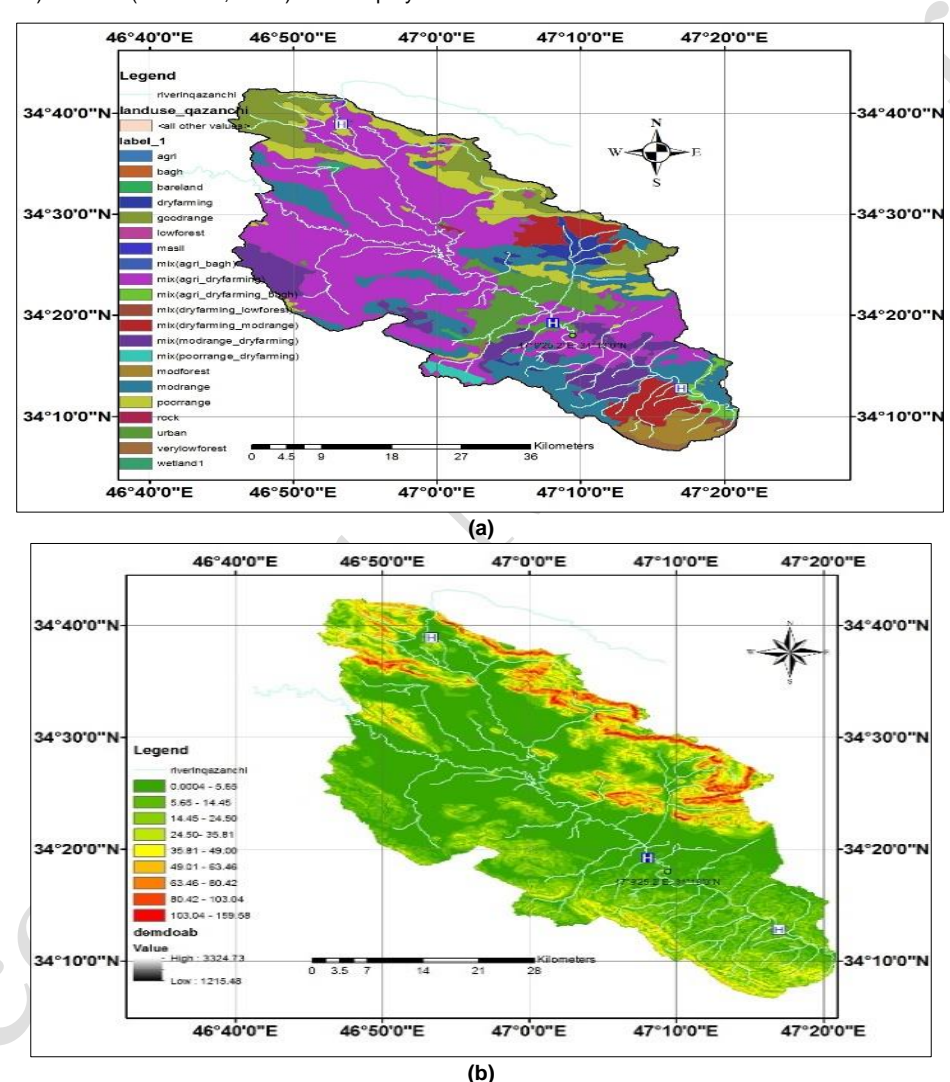


Fig. 3. Landuse map (a) and slop map (b) for the study area.

The DEM and other key components of flood magnitude mapping were examined using Hec Geo Ras that is specialized ArcGIS extension, facilitates the handling of geospatial data with HEC-RAS. Users can generate a Hec Geo Ras import sample with geometric attribute data from an existing DTM and additional datasets. Additionally, the extension enables processing of water surface profile results to visualize flood inundation depths and boundaries. Hec Geo Ras extension serves as an interface to establish a direct connection for transferring information between ArcGIS and Hec Ras (Desalegn and Mulu, 2021). The length of the studied river reach is about 16,500 meters. The plan of sections used in the simulation of the mentioned flood in Hec Geo Ras is shown in Fig.

4. The Hec Geo Ras model results are influenced by the chosen time step (Δt). Using a small time step increases computation time. In this study, a one-hour time step was chosen because the volumes under the input hydrograph, the river's exit hydrograph, and those in intermediate sections are nearly identical. Terrain data provide a physical representation of the area.

The Hec Geo Ras model develops a hydraulic simulation of floods, generating maps that display flood speed, height, and duration. The Manning's coefficient varies between 0.025 and 0.05 across different sections of the river. Finally, the model's results are compared to actual data from Sentinel imagery.

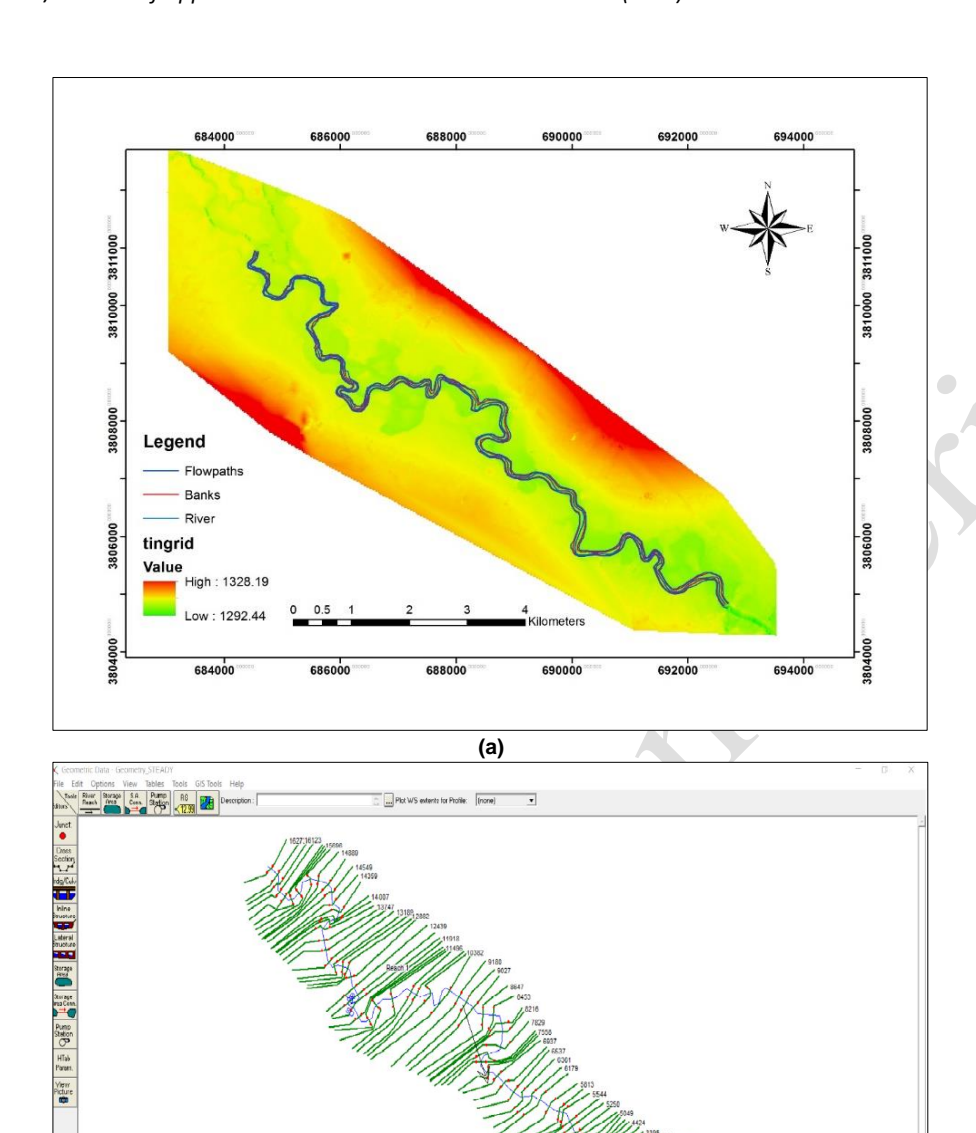


Fig. 4.(a) DEM and River component, (b) Plan of the studied river sections in HEC GEO RAS.

2.3. SAR techniques for the detection of flood plain area

This study utilized Sentinel-1 data acquired on April 06, 2019, three days post the flood on April 3, 2019. The Sentinel-1 sensor, owned by the European Space Agency (SciHub; https://scihub.copernicus.eu), was launched in 2014 and is accessible on Sentinel's online platform, with a 12-day revisit cycle encompassing C-band (5.405 GHz). The radar satellites provide high geometric resolution (10 m) and dual-polarization (VH + VV). SAR systems act as active sensors in microwave wavelengths, with 2 cm microwaves (approx. 12 GHz) penetrating the atmosphere. This allows the sensors to capture images of Earth's surface through clouds, regardless of time of day (Cao *et al.*, 2019). Before delving into the various processing steps for SAR data enhancement, it's essential to understand the significance of each stage in improving the overall quality and accuracy of the images. Due to the lack of ground truth data during the flood event, the threshold was determined empirically by analyzing the backscatter histogram of water and non-water pixels. A fixed threshold

(e.g., -3 dB for VH polarization) was chosen based on established literature for water detection in SAR imagery (Cao *et al.*, 2019). Sensitivity analysis was performed to validate the robustness of the selected threshold.

1-Apply Orbit Correction: supplies precise satellite position and velocity data, which updates the orbit state vectors in the product's abstract metadata. Precise orbit files are typically available days to week post-product generation. As this is an optional step, the tool will proceed with the workflow if the orbit file is unavailable, facilitating rapid mapping applications.

2-Thermal Noise Removal: Thermal noise correction is performed on uncorrected Sentinel-1 Level-1 GRD products.

3-Radiometric Calibration: The goal of SAR calibration is to ensure that pixel values accurately reflect the radar backscatter of the scene. While uncalibrated SAR imagery is adequate for qualitative analysis, calibrated images are crucial for quantitative assessment.

4-Speckle Filtering: SAR images exhibit a texture known as speckles, which can diminish image quality and complicate feature interpretation. These speckles result from random constructive and destructive interference of de-phased yet coherent return waves scattered by elementary scatters within each resolution cell. Speckle noise reduction can be achieved through spatial filtering or multilook processing, with a Lee filter of size 5x5 applied in this step. Orbit correction and radiometric aclibration are critical preprocessing steps to ensure geometric and radiometric accuracy, reducing distortions and biases in backscatter values. While their direct impact on flood detection accuracy was not quantified here, these steps are standard in SAR-based flood mapping to mitigate errors from terrain effects and sensor noise

5-Terrain Correction: Topographical variations and the satellite sensor's tilt can distort distances in SAR images. Areas not directly aimed at the sensor's nadir location will experience distortion. Terrain corrections are applied to compensate for these inaccuracies, ensuring a realistic geometric representation in the image. The Sentinel-1 dataset was hosted on the GEE platform to execute all necessary tasks for SAR satellite data processing. Utilizing the GEE platform, tasks such as orbit correction, noise reduction, radiometric calibration, and terrain correction were performed using SRTM data. Additionally, the backscatter intensity was converted to decibels (dB) following Eq. 3.

$$\sigma^{\circ} = 10 * log_{10}^{\sigma^{\circ}} \tag{3}$$

Water regions were detected in SAR radar images using several methods, including interferometric coherence calculation (Chini et al., 2019), histogram thresholding techniques (Chini et al., 2017; Liang & Liu, 2020), a region growing algorithm and active contour mode (Teatini et al., 2012), and object-oriented classification (Horritt et al., 2001). This study utilized the histogram method to determine optimal threshold values for detecting water bodies. The histogram of the Sentinel-1 image displays intensity values, with bars indicating the frequency of various backscattering intensities per pixel. The valley between two peaks represents the backscattering coefficient threshold that differentiates water from non-water regions. Accurate threshold calculations are essential for identifying water areas using SAR data and often require comparison with other methods. We delineated a water region along a section of the Gharasoo River using Sentinel-2 color images as a reference, aiming to determine the most suitable SAR threshold. After processing and classifying the images in ArcGIS 10.2, the water area of the Gharasoo region, based on the Sentinel-2 image, was found to be 86 km², as depicted in Fig. 5.

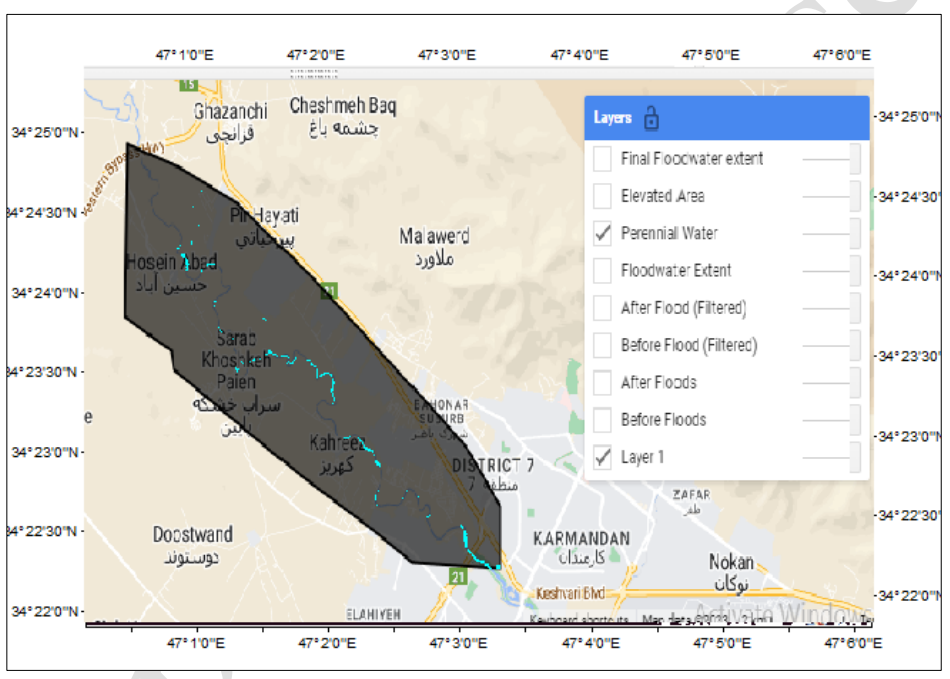


Fig. 5. Prennial water extraction for Gharasoo River in the GEE.

2.4. Optical sensors

Various techniques and indices are available for water zoning extraction from optical satellite imagery (Tobón-Marín and Barriga, 2020). The most commonly used indices for this purpose are the Normalized Difference Water Index (NDWI) (McFeeters, 1996), Modified Normalized Difference Water Index (MNDWI) (Xu, 2006), and the recently developed Automated Water Extraction Index (AWEI) (Feyisa et al., 2014) (Sinha et al., 2008; Martinis et al., 2013). The ability to detect water bodies in multispectral satellite imagery stems from the fact that increased surface moisture leads to decreased reflectance in the visible, near-infrared (NIR), and particularly short-wave infrared (SWIR) regions of the electromagnetic spectrum (Bach and Verhoef, 2003). By analyzing normalized differences in reflection coefficients, distinguishable water bodies can be identified based on their spectral characteristics. The NDWI is specifically designed to define water body boundaries, differentiate between water, soil, and vegetation, and assess water turbidity and pollution. It produces index values between 0 and 1, representing water bodies at various depths and contamination levels through a gradient of positive values (Eq. 4).

$$NDWI = \frac{\rho Green - \rho NIR}{\rho Green + \rho NIR} = \frac{\rho Band3 - \rho Band8}{\rho Band3 + \rho Band8}$$
 (4)

where, $\rho Green$ and ρNIR represent the reflection coefficients of electromagnetic radiation in the green and NIR spectral ranges, respectively. MNDWI enhances the visibility of open water bodies and reduces noise from urban areas, vegetation, and soils (Li *et al.*, 2022) in Eq. 5.

$$\mathsf{MNDWI} = \frac{\rho \mathsf{Green} - \rho \mathsf{SWIR}}{\rho \mathsf{Green} + \rho \mathsf{SWIR}} = \frac{\rho \mathsf{Band3} - \rho \mathsf{Band11}}{\rho \mathsf{Band3} + \rho \mathsf{Band11}} \tag{5}$$

where, $\rho SWIR$ represents the reflection coefficient of electromagnetic radiation in the SWIR range. The right side of the expressions corresponds to Sentinel-2 band numbers. Pixels were classified as "water" if NDWI > 0 or MNDWI > 0.

2.5. Accuracy assessment of HEC GEO RAS and satellite image water extent

To evaluate the fit of raster layers from SAR images against the raster of overflowed zones recreated by Hec-RAS, we utilize two scales: feature agreement statistics F1 and F2, as defined in equations 6-7 by Horrit *et al.*, (2007) and Di Baldasarre *et al.*, (2009).

$$F1 = \frac{A}{A + B + C} \tag{6}$$

$$F2 = \frac{A-B}{A+B+C} \tag{7}$$

In these equations, A represents the total inundated area correctly predicted by the model (from the detected Sentinel-1 image), B is the area overestimated, and C is the area underestimated. F1 ranges from 0 to +1, while F2 ranges from -1 to +1. Higher values of F1 and F2 (greater than 0.5) indicate better model performance.

3. Results and discussion

3.1. HEC RAS simulation in steady state and unsteady state scenarios

Ability to model steady and unsteady flow, along with powerful graphics, has made Hec Geo Ras software one of the most practical tools in water engineering. The Table 2 displays the results of calculating flood discharge for various return periods with the most optimal distributions in EASY-FIT model (Schittkowski, 2002), additionally, the RFFA results for Doab Ghazanchi are presented in the last row of the Table 2. The changes in cross-sectional area and average velocity of the Gharasoo River for different return periods of discharge are shown in Fig. 6-a, b. Longitudinal profiles of water surface elevation are among the valuable outputs of the HEC-RAS model. Therefore, after running the flow simulation model, the

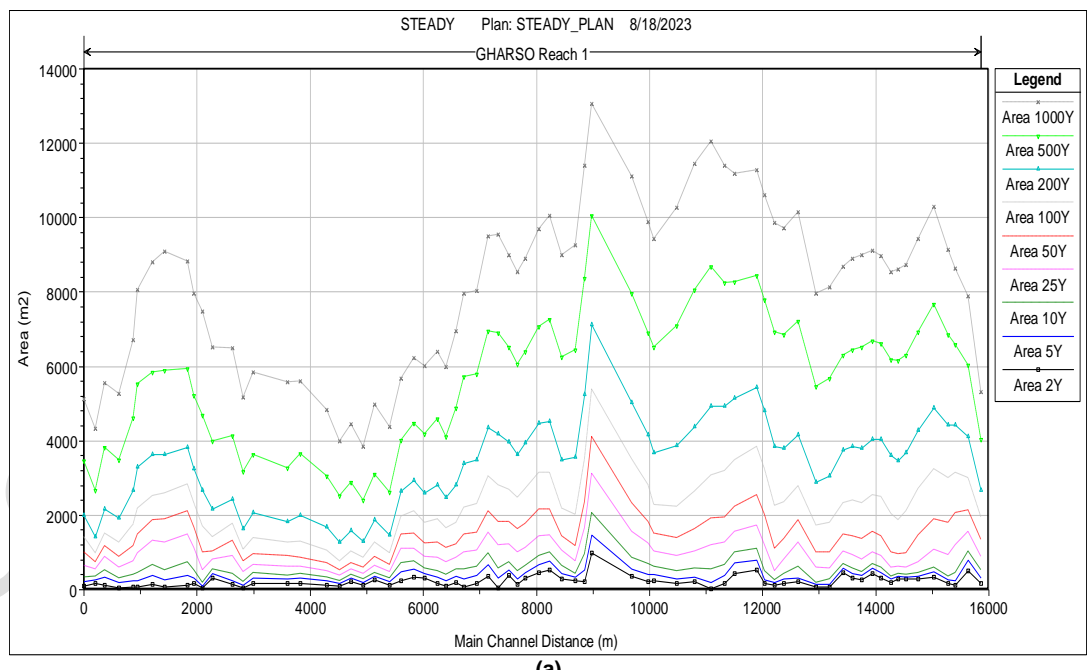
longitudinal profiles of water surface elevation changes for flood events with DRP, were extracted and presented in Fig. 6c. The average cumulative rainfall recorded at Kermanshah and Ravansar synoptic stations between 31/03/2019 and 2/04/2019, shown in Fig. 7a, was used for runoff simulation. The upstream basin of the study area covers 4590 sq km, with a concentration time of 30 h. A CN value of 73 was identified as optimal for the analysis (Fig. 3). The resulting hydrograph depicting the flood caused by the rainfall event is displayed in Fig. 7-b (Hafezparast, Gord, Ghobadian, 2025). The simulated SCS peak flood in Doab-Ghazanchi was estimated at 860.25 m³/s (Fig. 7b). Findings indicated that the 25-year peak flood, at 723.5 m³/s using the RFFA method in Doab Ghazanchi, is lower than the SCS method in this region.

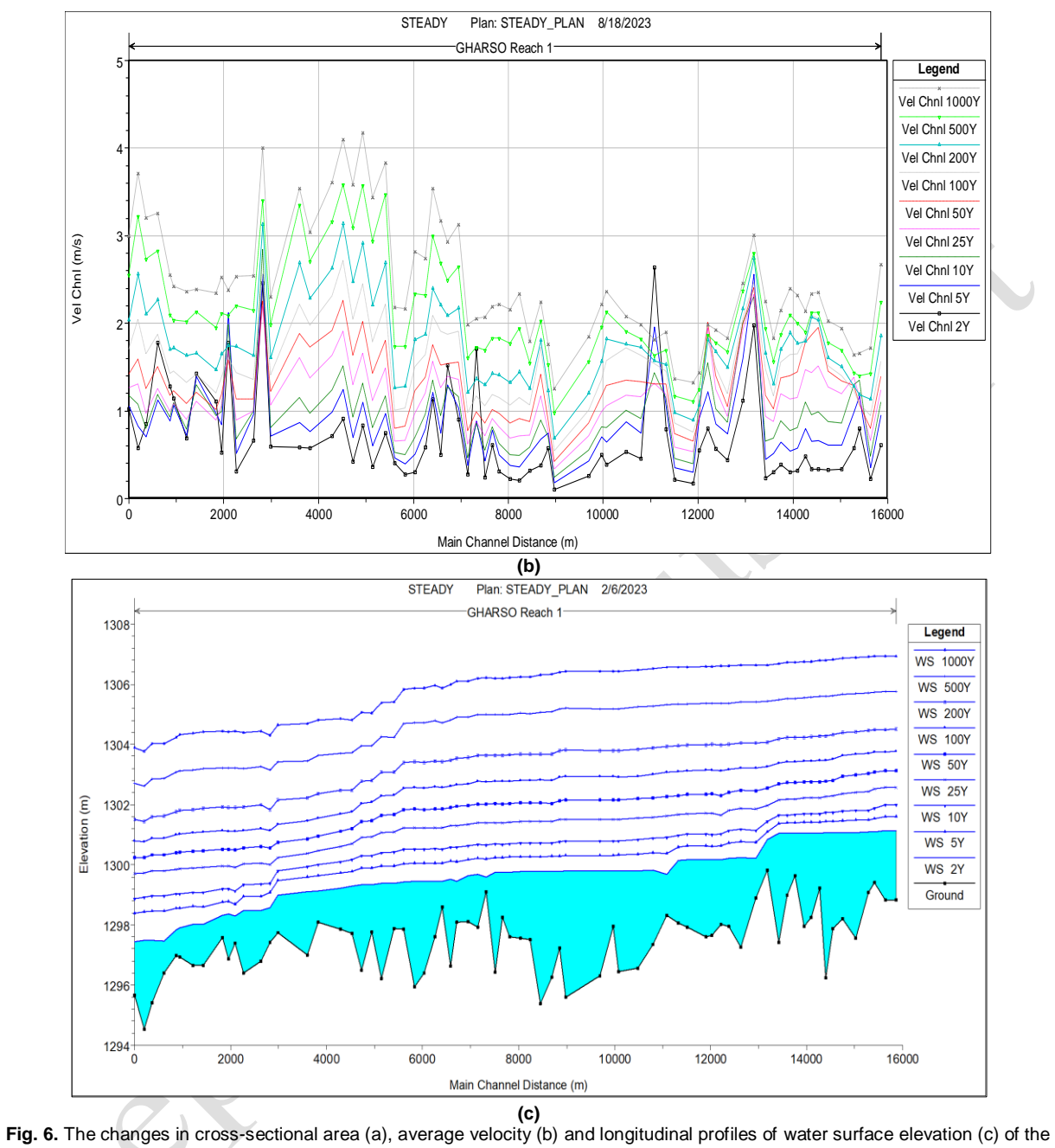
3.2. Water level and velocity of flood in the Hec Geo Ras

HEC GEO RAS model simulated the variations in water level profiles for steady and un steady states, including flow velocity, normal depth, critical depth, and hydraulic parameters. Water level and velocity maps are categorized into four and five groups in a GIS environment and shown in Figs. 8a, b - 9a, b. The simulated water heights reached over 4 m in the riverbed and between 1 and 2 m on the floodplain. In Kermanshah city, the water level is estimated at 1 m, with a maximum height of 6 m and a maximum velocity of 3 m/s.

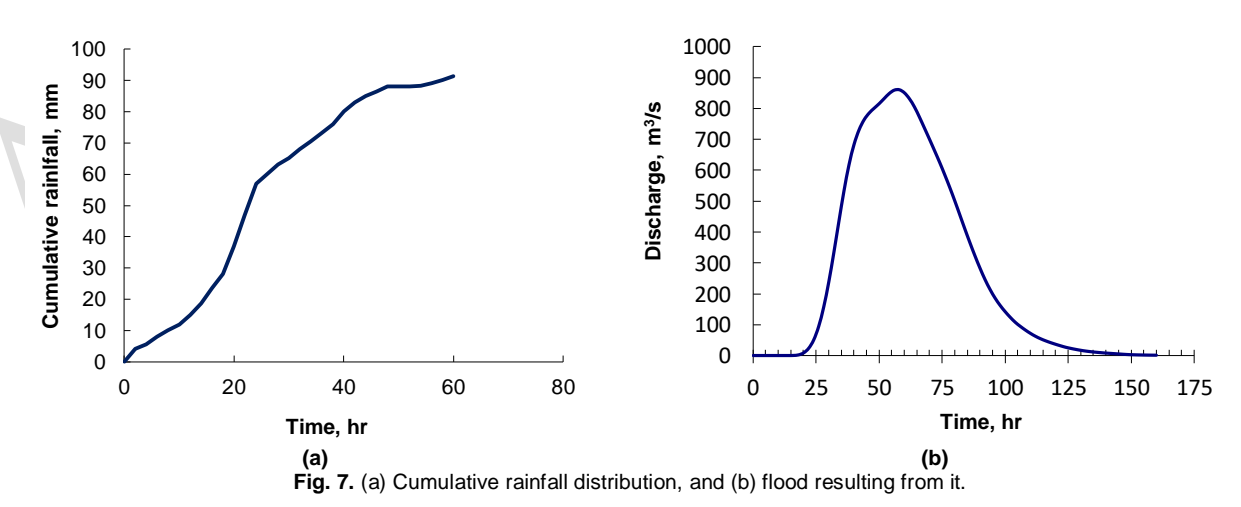
Table 2. Predicted Discharge with the best distribution in hydrometric stations and RFFA in Doab-Ghazanchi area.

Stations	Best distribution	Return period, Year									
Stations		2	3	5	10	25	50	100	200	500	1000
Doab merek	Lognormal (3P)	33.8	51.7	80.9	128.6	211.4	291.5	389.5	507.9	700.7	878.3
Khersabad	Lognormal (3P)	37.5	52.5	72.9	100.8	141.0	174.4	210.6	250.0	307.2	354.7
Hojatabad	Frechet 3p	76.2	104.6	147.9	217.1	340.7	468.5	637.1	859.8	1268.3	1695.3
Pol-kohne	log-logistic 3p	100.5	149.9	236.9	402.5	775.1	1256	2026.4	3263.6	6121.5	9849.6
Faraman	log_person3	107.1	160.1	247.6	395.2	665.3	943.1	1302	1761.4	2563.9	3356.7
Doab-Ghazanchi	RFFA	93.8	139.9	221.1	375.6	723.5	1172.3	1891.3	3046.1	5713.5	9193.1





Gharasoo River for different return periods.



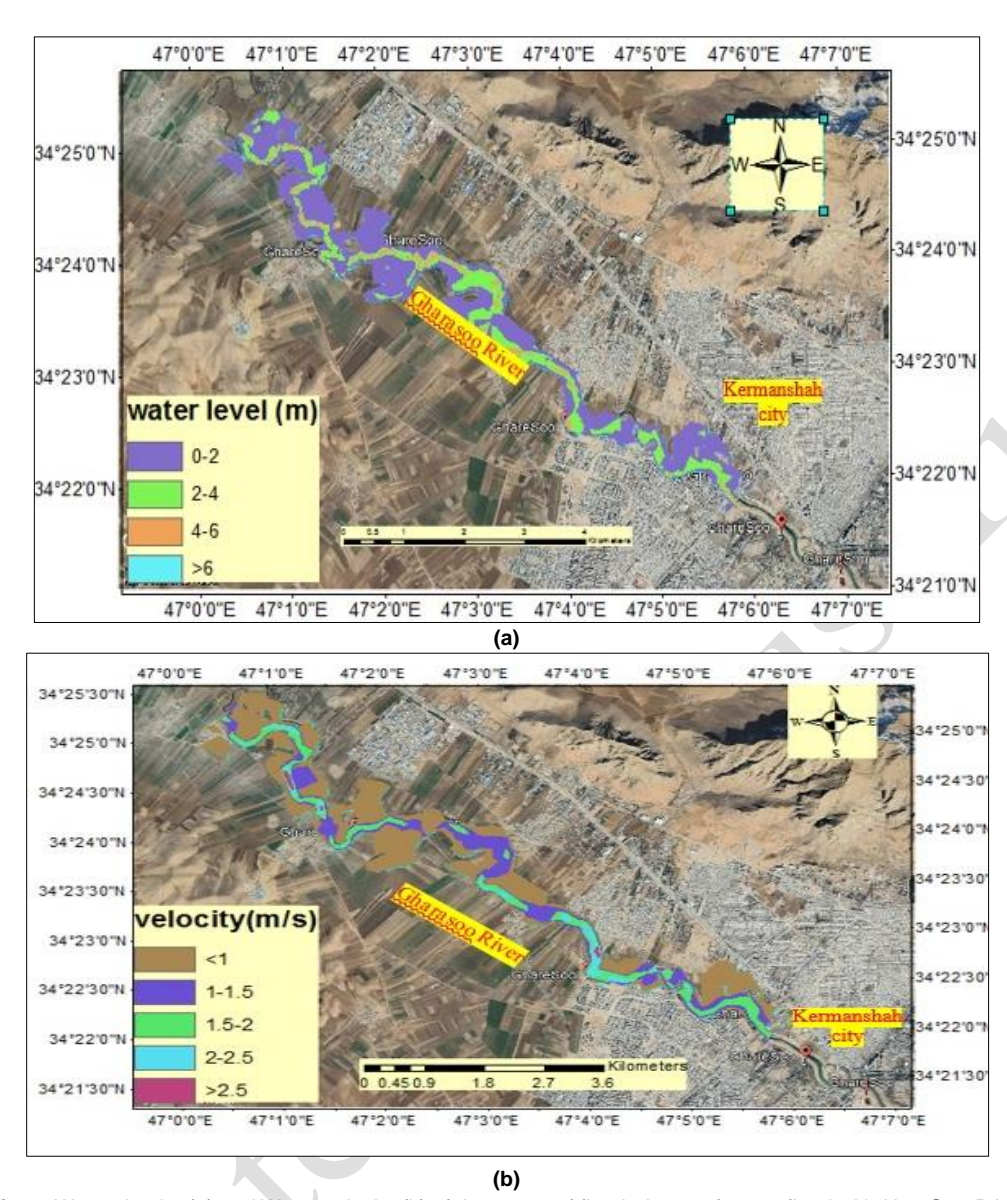


Fig. 8. Water depths (a) and Water velocity (b) of the extent of flooded areas for 25y flood with Hec-Geo-RAS.

3.3. Satellite images processing in GEE

The images related to the Sentinel 2 satellite on 04/04/2019 that is on the exact flooded day, was very cloudy due to the heavy rain, and with the filters applied to remove the cloud, the quality was still not good that is obvious in Fig. 10.

Landsat image was acquired on 15/04/2019 that was about 11 days after flood but still it showed the flooded area that is clear in Fig.11. The Sentinel 1 image from 06/04/2019, acquired 2 days post-flood and unaffected by clouds, is more suitable for comparison with the Hec-Geo-RAS model output. This image is shown in Fig.12 for further study in this area.

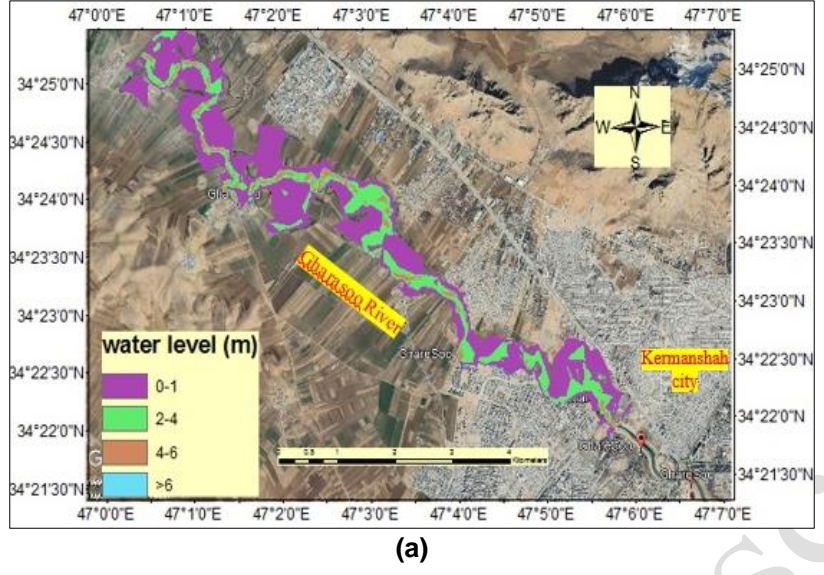
3.4. Evaluating Hec-Geo-RAS simulation and satellite images

Sentinel-1 images on GEE are utilized for data processing, cloud and speckle filtering, and automated water detection threshold (Parida et al.,

2021) in comparison to the Hec Geo Ras model. The maximum 25-year flood for steady state conditions and the SCS flood hydrograph for unsteady state scenarios are assessed using satellite imagery. Water areas in the S1 satellite image and Hec Geo Ras SCS floodplain are overlaid in a GIS environment, and the coefficients of A, B, and C are extracted, as shown in Fig.13 and Table 3. F1 and F2 indices for the Max SCS flood exhibited values of 0.73 and 0.72, indicating that the Hec-Geo-RAS water plains were well-aligned with the S1 satellite images for unsteady scenario. Conversely, the evaluation indices F1 and F2 indicated that the SCS flood in Non-state scenario overlapped more with the satellite images compared to the 25y flood in steady state scenario. Studies by Karkouti et al., (2010) on the flood of 19/03/1998, Jahandideh et al., (2011) on the flood of 29/03/2005, and Jabbari et al., (2017) estimating the maximum flood in the Ghazanchi area using Creager, HEC HMS, SCS and probabilistic distribution methods indicate that the peak flow ranges from 720 to 900 m³/s, aligning with this study.

Table 3. Evaluation Factors in steady state and unsteady state scenarios.

	Table 3. Evaluation Factors in s	steady state at	iu uristeauy s	state scenanos		
Satellite imagery	Hec-Geo-RAS simulation	Α	В	С	F1	F2
	scenarios Number of pixels					
Sentinel-1	Unsteady state	40896	211	15105	0.73	0.72
Sentinei-1	steady state	29786	9472	32646	0.41	0.28



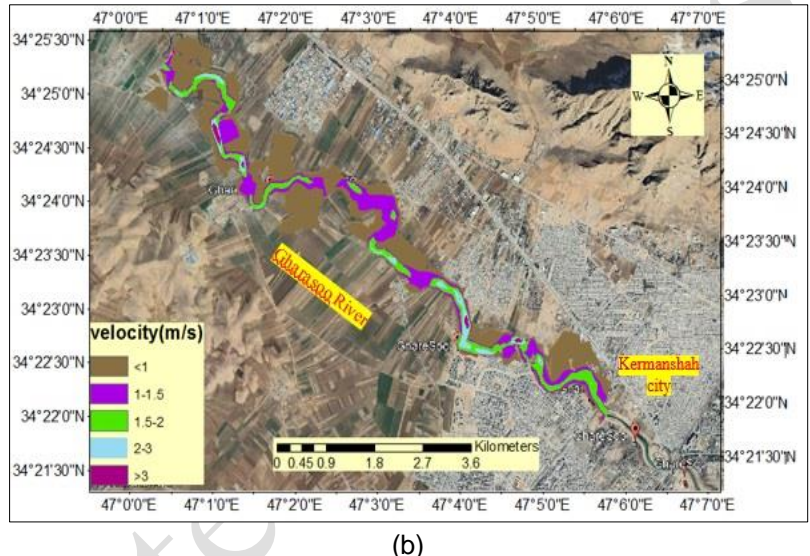
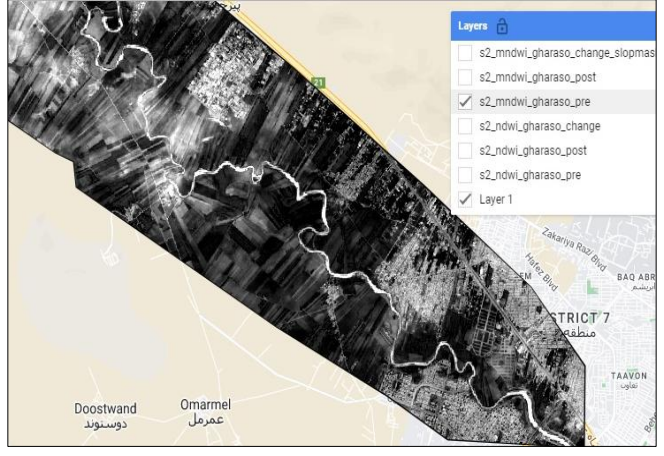
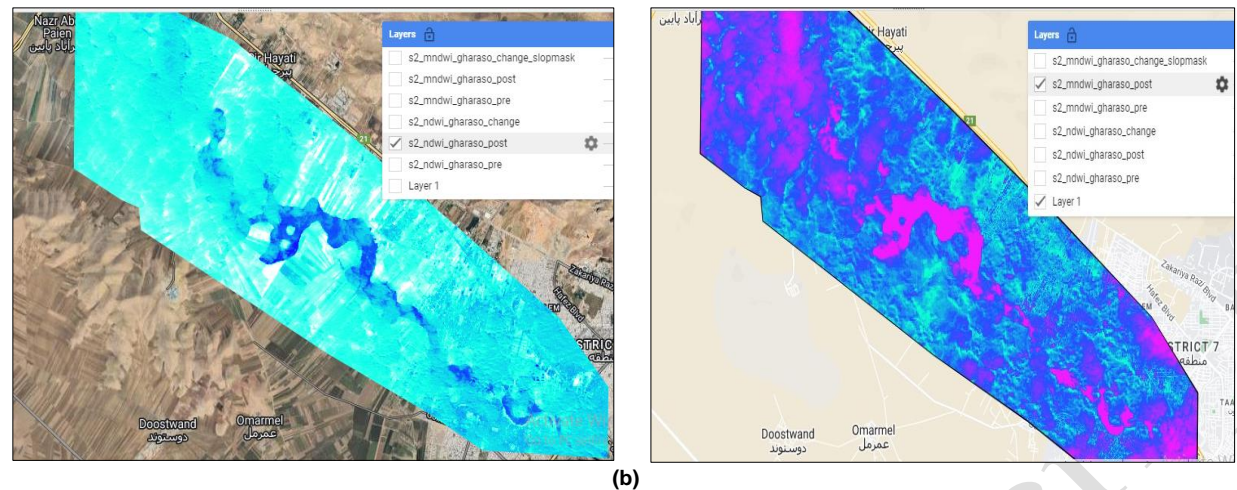


Fig. 9. (a) Water depth, and (b) water velocity of the maximum flood of the SCS method in the Hec-Geo-RAS.

Simulated water levels and velocities were measured during a flood, with heights surpassing 4m in the riverbed and peaking at 6m with a maximum velocity of 3ms-1. A comparison to Ezzine et al., (2020) reveals strong agreement between Hec Geo Ras and the observed flood extents seen in Sentinel-1 images. Water levels ranged from 1 to 6m, while

velocities ranged from 1 to 4ms-1 in the Medjerda Basin in northern Tunisia. This data is important for assessing flood risks and can aid decision-makers in understanding factors such as height, velocity, and flow duration.





(b)

Fig. 10. (a) Sentinel-2 acquired in March 2019 before flood, (b) NDWI and MNDWI in April 2019 after flood in the GEE platform in the Gharasoo River.

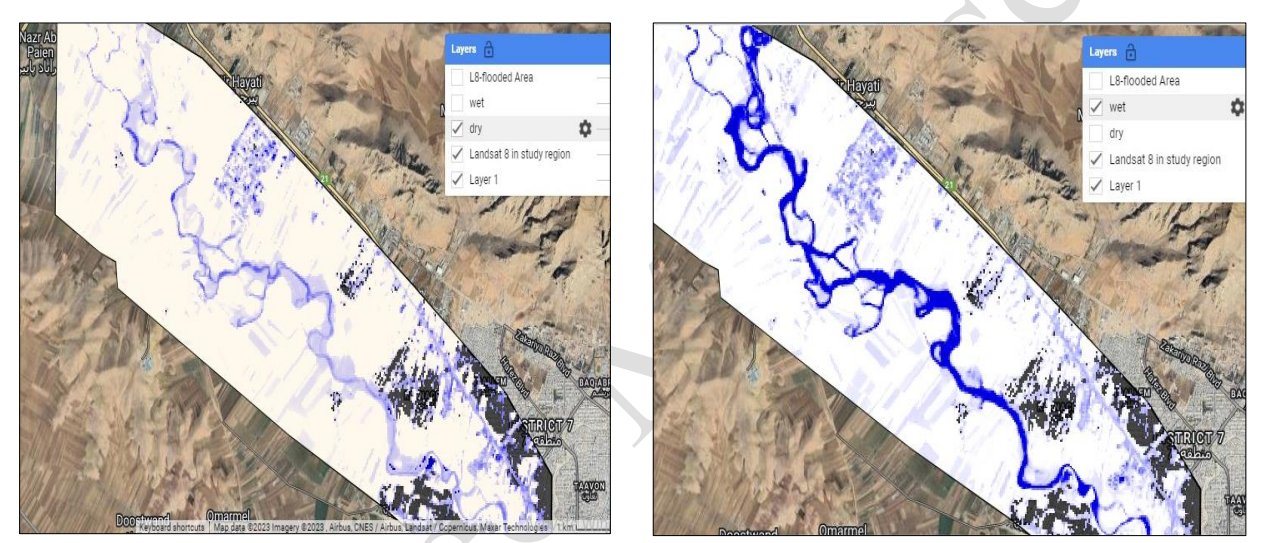
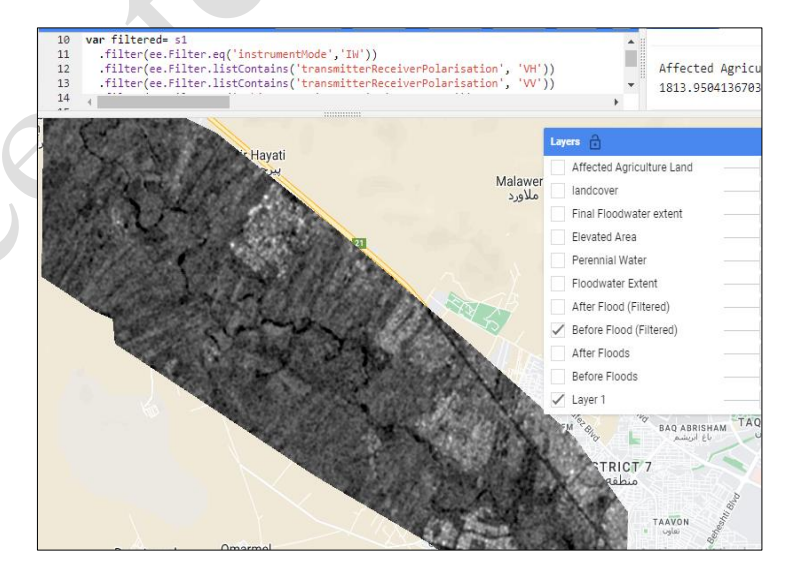


Fig. 11. Landsat-8 acquired in March 2019 before flood (Left) and in April 2019 after flood (Right) in the GEE platform in the Gharasoo River.



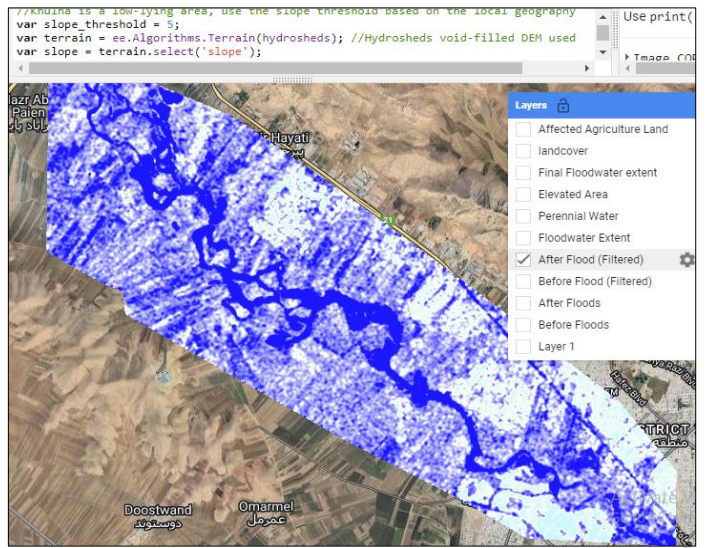
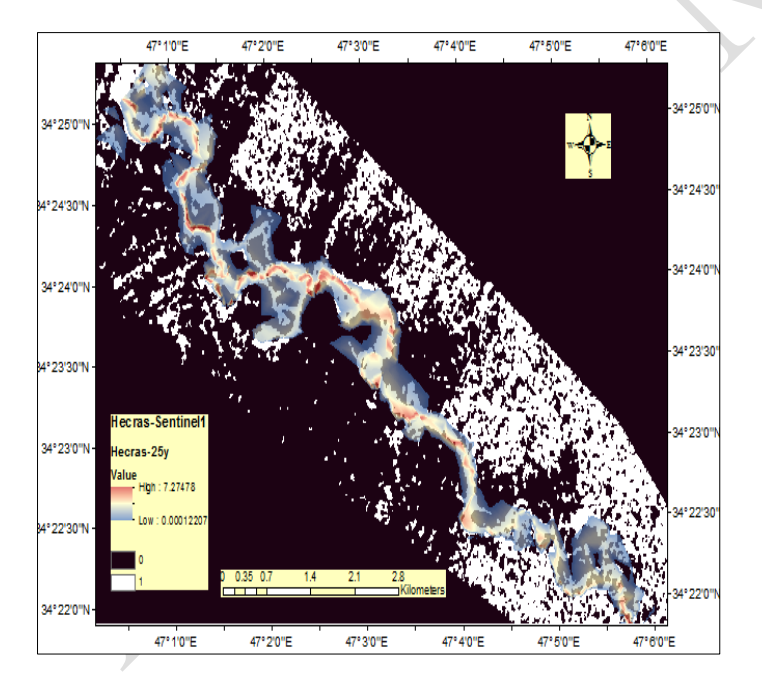
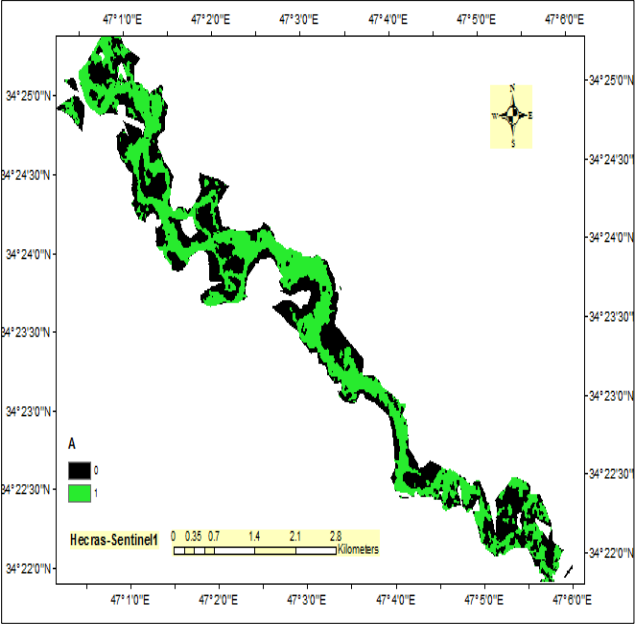


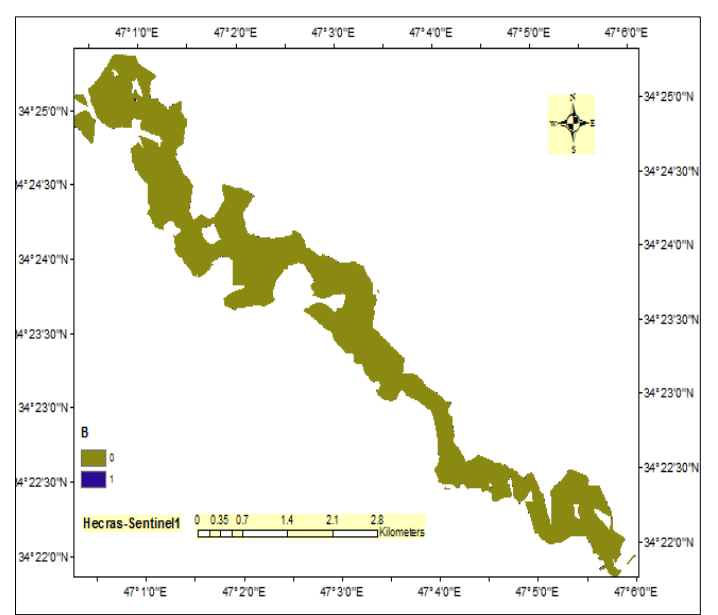
Fig. 12. Sentinel-1 data VH polarization and acquired in March 2019 before flood (up) and in April 2019 after flood (down) in GEE platform in the Gharasoo River.

Issues concerning SAR images include signal scattering when signals bounce off surfaces and sensors fail to pick them up. Dark areas don't always mean flooded areas, and uncertainties can affect results. Satellite images may not be available for all locations simultaneously, causing a delay between flooding and image capture. SAR images encounter challenges due to signal scattering during reflection and reception. We employed the thresholding method to extract flooded areas from pre- and post-flood Sentinel-1 images, achieving agreement values of 72% and 73% for VH polarizations. This approach is straightforward, quick, and reliable for flood mapping. In comparison with studies on optimal thresholds for identifying water areas, Elkhrachy *et al.*, (2021) reported a similarity of 74.2% to 89.7% between simulated HEC-RAS

water areas and SAR data, while Hong Quang et al., (2020) noted the highest agreement of 88.3% between water levels and calibrated water extent using HEC-RAS 2D. Ezzin et al., (2020) evaluated the performance of HEC-RAS using S1 satellite images by calculating F1 and F2 values, which both exceeded 0.5. Afzal et al., (2022) discovered that proper calibration and validation of HEC-RAS inundation modeling with in situ flood extent is crucial. Achieving this during a catastrophic flood may be challenging. However, using MODIS and Landsat data for flood extent comparison has proven beneficial. The calibration and validation results show strong agreement between simulated and observed flood extents in most areas, with the model achieving an accuracy of 0.64 for F1 and 0.87 for F2.







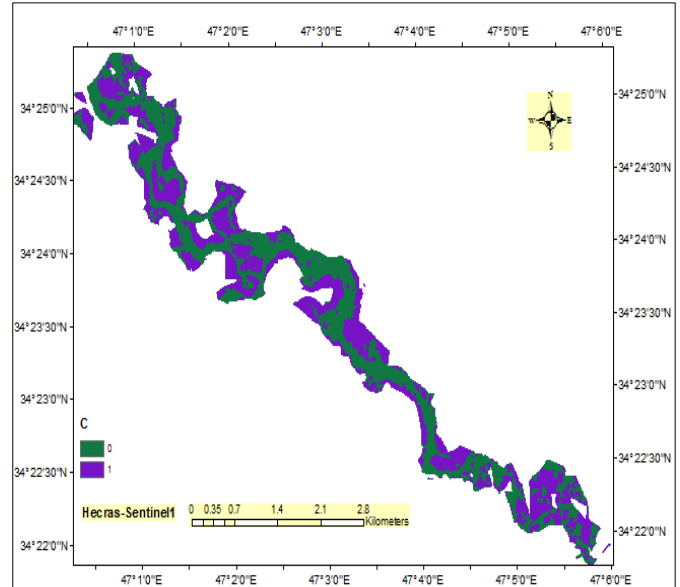


Fig. 13. Extraction of A, B, and C components of F-statistic scales between Hec-Geo-RAS and SAR satellite image water areas for maximum SCS flood.

4. Conclusions

In this research, a flood event simulated in April 2019 focusing on the Doab-Ghazanchi section upstream of Kermanshah city in western Iran. Peak flood and flood hydrograph were calculated using the RFFA and SCS methods and simulated in Hec Geo Ras for steady-state and unsteady-state scenarios. The results indicated that the 25-year flood and SCS peak flood values were estimated to be 723.5 m3/s and 860 m3/s, while the maximum water level and velocity were modeled at around 6 m and 3 m/s. GEE Satellite imagery analysis revealed that on the specific day of the flood, 04/04/2019, the Sentinel 2 images were heavily obscured by clouds caused by intense rain. Despite efforts to eliminate the cloud cover using filters, the image quality remained inadequate. Landsat images obtained on 15/04/2019, approximately 11 days after the flood, were compared. Considering this, the Sentinel 1 images from 06/04/2019, captured just two days after the flood and free from cloud interference, offer a more appropriate basis for comparison with the Hec-Geo-RAS model results. Assessing the Hec-Geo-RAS model with S1 satellite images using F1 and F2 indices showed values of 0.73 and 0.72 for the max SCS flood, indicating good alignment with S1 flood plain. For the 25year flood in a steady state scenario, the values were 0.41 and 0.28, reflecting poor alignment. The analysis suggests that the unsteady state scenario in Hec-Geo-RAS, which employs the flood hydrograph to identify flood plains, is more appropriate than using peak flood value in the RFFA method for steady state scenarios. The results demonstrated the critical importance of properly simulating HEC-RAS inundation modeling with in situ flood extent needs. However, this may be difficult to accomplish during a catastrophic flood event. The use of satellite-based flood extent proved to be valuable for comparing simulated and actual floodplains.

Nomenclature	
AWEI	Automated water extraction index
CN	Curve number
DEM	Digital elevation model
DTM	Digital terrain model
FLOMPY	Flood mapping python toolbox
GEE	Google earth engine
GIS	Geographic information systems
MNDWI	Modified normalized difference water index
NDVI	Normalized difference vegetation index
NDWI	Normalized difference water index
RFFA	Regional flood frequency analysis
SAR	Synthetic aperture radar

Conflict of Interest

The authors declare that they have no known competing financial interests or personal relationships that could have appeared to influence the work reported in this paper.

Acknowledgement

The authors thank to ESA's Copernicus program, European Union, for making high-resolution (10m) satellite images freely available to the public.

Data Availability Statement

The S1 and S2 data from the real case were taken from the GEE platform (https://code.earthengine.google.com/) and the code for computing water area is available inhttps://github.com/maryamhafezparast/Google-Earth-Engin/gharasoo floodplain.

Author Contributions

Maryam Hafezparast: Supervision, validation, writing-original draft, review and editing, and methodology. Sadaf Gord: Conceptualization, investigation. Rasool Ghobadian:, analysis. Review and editing.

References

Afzal, M.A. et al. (2022) 'Flood inundation modeling by integrating HEC–RAS and satellite imagery: A case study of the Indus River basin', Water, 14(19), 2984. doi: https://doi.org/10.3390/w14192984

Avarand, Y. et al. (2025) 'Multi-objective fuzzy-stochastic optimization model for agricultural water allocation by applying effective rainfall', Sustainable Water Resources Management, 11(3), 66. doi: https://doi.org/10.1007/s40899-025-01243-2

Ayoubikia, R. et al. (2019) 'Optimization of regional water resources allocation in Sefidroud river basin by social equity approach', *Iran-Water Resources Research*, 14(5). pp. 236-252. doi: https://www.iwrr.ir/article_66470.html (Accessed date: 2 June 2025).

Bach, H. and Verhoef, W. (2003) 'Sensitivity studies on the effect of surface soil moisture on canopy reflectance using the radiative transfer model GeoSAIL', in *Proceedings of the 2003 IEEE International Geoscience and Remote Sensing Symposium (IGARSS 2003)*. Toulouse, France, 21-25 July 2003. Piscataway, NJ: IEEE, pp. 1679-1681

Brivio, P.A. et al. (2002) 'Integration of remote sensing data and GIS for accurate mapping of flooded areas', International Journal of Remote

- Sensing, 23(3), pp. 429–441. doi: https://doi.org/10.1080/01431160010014729
- Brown, K.M., Hambridge, C.H. and Brownett, J.M. (2016) 'Progress in operational flood mapping using satellite synthetic aperture radar (SAR) and airborne light detection and ranging (LiDAR) data', *Progress in Physical Geography: Earth and Environment*, 40(2), pp. 196–214. doi: https://doi.org/10.1177/0309133316633570
- Gao, B. (1996) 'NDWI—A normalized difference water index for remote sensing of vegetation liquid water from space', *Remote Sensing of Environment*, 58(3), pp. 257–266. doi: https://doi.org/10.1016/S0034-4257(96)00067-3
- Cao, H. et al. (2019) 'Operational flood detection using Sentinel-1 SAR data over large areas', Water, 11(4), p. 786. doi: https://doi.org/10.3390/w11040786
- Chen, Z. et al. (2019) 'RFim: a real-time inundation extent model for large floodplains based on remote sensing big data and water level observations', Remote Sensing, 11(13), p. 1585. doi: https://doi.org/10.3390/rs11131585
- Chini, M. et al. (2017) 'A hierarchical split-based approach for parametric thresholding of SAR images: Flood inundation as a test case', IEEE Transactions on Geoscience and Remote Sensing, 55(12), pp. 6975– 6988. doi: https://doi.org/10.1109/TGRS.2017.2737663
- Chini, M. et al. (2019) 'Sentinel-1 InSAR coherence to detect floodwater in urban areas: Houston and hurricane Harvey as a test case', *Remote Sensing*, 11(2), 107. doi: https://doi.org/10.3390/rs11020107
- Cunnane, C. (1998) 'Methods and merits of regional flood frequency analysis', *Journal of Hydrology*, 100(1-3), pp.269–290. doi: https://doi.org/10.1016/0022-1694(88)90188-6
- Desalegn, H. and Mulu, A. (2021) 'Mapping flood inundation areas using GIS and HEC-RAS model at Fetam River, Upper Abbay Basin, Ethiopia', *Scientific African*, 12, p. e00834. doi: https://doi.org/10.1016/j.sciaf.2021.e00834
- Di Baldassarre, G., et al. (2009) 'A technique for the calibration of hydraulic models using uncertain satellite observations of flood extent', *Journal of Hydrology*, 367(3-4), pp. 276–282. doi: https://doi.org/10.1016/j.jhydrol.2009.01.020
- Elkhrachy, I. (2021) 'Sentinel-1 remote sensing data and Hydrologic Engineering Centres River Analysis System two-dimensional integration for flash flood detection and modelling in New Cairo City, Egypt', *Journal of Flood Risk Management*, 14(2), p. e12692. doi: https://doi.org/10.1111/jfr3.12692
- Ezzine, A. et al. (2020) 'Flood mapping using hydraulic modeling and Sentinel-1 image: Case study of Medjerda Basin, northern Tunisia', *The Egyptian Journal of Remote Sensing and Space Science*, 23(3), pp. 303–310. doi: https://doi.org/10.1016/j.ejrs.2020.01.001
- Feyisa, G.L. et al. (2014) 'Automated water extraction index: A new technique for surface water mapping using Landsat imagery', Remote Sensing of Environment, 140, pp. 23–35. doi: https://doi.org/10.1016/j.rse.2013.08.029
- Gharbi, M. (2016) 'Etude des crues et du transport sédimentaire associé Application au bassin versant de la Medjerda'. Doctoral thesis. Université de Toulouse. Available at: https://oatao.univ-toulouse.fr/18120/ (Accessed: 2 April 2025).
- Giustarini, L. et al. (2013) 'A change detection approach to flood mapping in urban areas using TerraSAR-X', IEEE Transactions on Geoscience and Remote Sensing, 51(4), pp. 2417–2430. doi: https://doi.org/10.1109/TGRS.2012.2210901
- Gord, S., Hafezparast Mavaddat, M. and Ghobadian, R. (2024) 'Flood impact assessment on agricultural and municipal areas using Sentinel-1 and 2 satellite images (case study: Kermanshah province)', Natural Hazards, 120, pp. 8437–8457. doi: https://doi.org/10.1007/s11069-024-06514-3
- Hafezparast, M., Gord, S. and Ghobadian, R. (2025) 'Comparing random forest flood frequency analysis with regional flood frequency, Creager and SCS in Doab-Qazanchi, Kermanshah', *Journal of Applied*

- Research in Water and Wastewater, 12(1), pp. 86-95, doi: https://doi.org/10.22126/arww.2025.11095.1349
- Henry, J.B. et al. (2006) 'Envisat multipolarized ASAR data for flood mapping', International Journal of Remote Sensing, 27(9-10), pp. 1921–1929. doi: https://doi.org/10.1080/01431160500486724
- Hong Quang, N. et al. (2020) 'Hydrological/hydraulic modeling-based thresholding of multi SAR remote sensing data for flood monitoring in regions of the Vietnamese Lower Mekong River Basin', Water, 12(1), p. 71. doi: https://doi.org/10.3390/w12010071
- Horritt, M.S. et al. (2007) 'Comparing the performance of a 2-D finite element and a 2-D finite volume model of floodplain inundation using airborne SAR imagery', *Hydrological Processes*, 21(20), pp. 2745–2759. doi: https://doi.org/10.1002/hyp.6486
- Horritt, M.S. et al. (2001) 'Flood boundary delineation from synthetic aperture radar imagery using a statistical active contour model', International Journal of Remote Sensing, 22(13), pp. 2489–2507. doi: https://doi.org/10.1080/01431160116969
- ICLR (2019) Focus on flood mapping in Canada. Canada. Institute for Catastrophic Loss Reduction Available at: https://www.iclr.org/wp-content/uploads/2019/11/ CatTales Sept-Oct-2019.pdf (Accessed: date 2 June 2025).
- Li, M. et al. (2022) 'Automated extraction of lake water bodies in complex geographical environments by fusing sentinel-1/2 Data', Water, 14(1), p. 30. doi: https://doi.org/10.3390/w14010030
- Liang, J. and Liu, D. (2020) 'A local thresholding approach to flood water delineation using Sentinel-1 SAR imagery', *ISPRS Journal of Photogrammetry and Remote Sensing*, 159, pp. 53–62. doi: https://doi.org/10.1016/j.isprsjprs.2019.10.017
- Liu, X. et al. (2017) 'Flood inundation mapping from optical satellite images using spatiotemporal context learning and modest AdaBoost', Remote Sensing, 9(6), p. 617. doi: https://doi.org/10.3390/rs9060617
- Martinis, S. et al. (2013) 'A multi-scale flood monitoring system based on fully automatic MODIS and TerraSAR-X processing chains', Remote Sensing, 5(11), pp. 5598–5619. doi: https://doi.org/10.3390/rs5115598
- McFeeters, S.K. (1996) 'The use of the Normalized Difference Water Index (NDWI) in the delineation of open water features', *International Journal of Remote Sensing*, 17(7), pp. 1425–1432. doi: https://doi.org/10.1080/01431169608948714
- Notti, D. et al. (2018) "Potential and limitations of open satellite data for flood mapping". Remote Sensing, 10(11), 1673. doi: https://doi.org/10.3390/rs10111673
- Parida, B.R. et al. (2021) 'Estimating floodwater depth using SAR-derived flood inundation maps and geomorphic model in kosi river basin (India)', Geocarto International, 37(16), pp. 4665–4690. doi: https://doi.org/10.1080/10106049.2021.1899305
- Pulvirenti, L. et al. (2010) 'Analysis of COSMO-SkyMed observations of the 2008 flood in Myanmar', Italian Journal of Remote Sensing, 42(2), pp. 79–90. doi: https://doi.org/10.5721/ltJRS20104227
- Rosser, J.F. et al. (2017) 'Rapid flood inundation mapping using social media, remote sensing and topographic data', *Natural Hazards*, 87(1), pp. 103–120. doi: https://doi.org/10.1007/s11069-017-2755-0
- Schittkowski, K. (2002) 'EASY-FIT: a software system for data fitting in dynamical systems', *Structural and Multidisciplinary Optimization*, 23(2), pp. 153–169. doi: https://doi.org/10.1007/s00158-002-0177-3
- Schlaffer, S. et al. (2015) 'Flood detection from multi-temporal SAR data using harmonic analysis and change detection', *International Journal of Applied Earth Observation and Geoinformation*, 38, pp. 15–24. doi: https://doi.org/10.1016/j.jag.2014.12.001
- Shen, X. et al. (2019) 'Inundation extent mapping by synthetic aperture radar: a review', Remote Sensing, 11(7), p. 879. doi: https://doi.org/10.3390/rs11070879
- Sinha, R. et al. (2008) 'Flood risk analysis in the Kosi river basin, north Bihar using multiparametric approach of Analytical Hierarchy Process

- (AHP)', Journal of the Indian Society of Remote Sensing, 36(4), pp. 335–349. doi: https://doi.org/10.1007/s12524-008-0034-y
- Talbi, S. (2011) "Etude et modélisation de la propagation de l'onde de crue (cas de l'oued Medjerda-tronçon Jendouba-Bou Salem)-amélioration de modèle". Master's Thesis, Institut National Agronomique de Tunisie (INAT). Available at: http://www.umaxx.tn/handle/123456789/1080 (Accessed date: 4 June 2025).
- Teatini, P. et al. (2012) "Resolving land subsidence within the Venice Lagoon by persistent scattered SAR interferometry', *Physics and Chemistry of the Earth, Parts A/B/C*, 40–41, pp. 72–79. doi: https://doi.org/10.1016/j.pce.2010.01.002
- Tobo'n-Marı'n, A. and Can"o'n Barriga, J. (2020) 'Analysis of changes in rivers planforms using google earth engine', *International Journal of Remote Sensing*, 41(22), pp. 8654–8681. doi: https://doi.org/10.1080/01431161.2020.1792575
- Touihri, N. (2015) "Essai de reconstitution et de prévision des crues aux stations principales de la Medjerda à l'aval du barrage Sidi Salem (Tronçon Sidi Salem Slouguia Medjez el beb)". Master's Thesis, Institut National Agronomique de Tunisie (INAT). Available at: http://www.umaxx.tn/handle/123456789/1080 (Accessed date: 10 February 2025).
- U.S. Army Corps of Engineers (2016) "HEC-RAS River Analysis System Hydraulic Reference Manual". Version 5.0. Davis, CA: USACE. Available at: https://www.hec.usace.army.mil/software/hec-ras/documentation/HEC-RAS%205.0%20Reference%20Manual.pdf (Accessed date: 7 January 2025).
- Urzica, A. et al. (2018) 'Using GIS methods for modelling exceptional flood events in Baseu river basin, NE Romania". In: *Proceedings of the 4th International Scientific Conference Geobalcanica*. Skopje, Republic of Macedonia, pp. 463–471. Available at: https://geobalcanica.org/wp-

- content/uploads/GBP-2018-048.pdf (Accessed date: 16 January 2025).
- USDA (1986) 'Urban Hydrology for Small Watersheds". 2nd ed. Technical Release 55 (TR-55). Washington, D.C.: Natural Resources Conservation Service, Conservation Engineering Division. Available at: https://www.nrcs.usda.gov/Internet/FSE_DOCUMENTS/stelprdb10 44171.pdf (Accessed date: 14 July 2025).
- Wulder, M.A. et al. (2012) 'Opening the archive: How free data has enabled the science and monitoring promise of Landsat', Remote Sensing of Environment, 122, pp. 2–10. doi: https://doi.org/10.1016/j.rse.2011.06.022
- Xu, H. (2006) 'Modification of normalized difference water index (NDWI) to enhance open water features in remotely sensed imagery', *International Journal of Remote Sensing*, 27(14), pp. 3025–3033. doi: https://doi.org/10.1080/01431160600589179
- Yamada, Y. (2001) 'Detection of flood-inundated area and relation between the area and micro-geomorphology using SAR and GIS". In: Proceedings of the IGARSS 2001–2001 IEEE International Geoscience and Remote Sensing Symposium. Sydney, NSW, Australia, 9–13 July 2001, 7, pp. 3282–3284. doi: https://doi.org/10.1109/IGARSS.2001.978285
- Zotou, I. et al. (2022) 'Potential of two sar-based flood mapping approaches in supporting an integrated 1D/2D HEC-RAS model', Water, 14(24), p. 4020. doi: https://doi.org/10.3390/w14244020
- Zotou, I. et al. (2020) 'Using sentinel-1 imagery to assess predictive performance of a hydraulic model', Water Resources Management, 34(14), pp. 4415–4430. https://doi.org/10.1007/s11269-020-02592-7